Supplementary Material

Complexity Reveals the Microscopic Drivers of Macroscopic Dynamics

Haoyang Qian[1], Beata Casiday[2], Gabriel Hood[3], and Malbor Asllani[1*]
[1] *Department of Mathematics, Florida State University, Tallahassee, FL, USA*
[2] *Yale University, New Haven, CT, USA and*
[3] *Georgia Institute of Technology, Atlanta, GA, USA*

I. LOCALIZED–SPECTRAL MEASURES FOR THE GRAPH LAPLACIAN EIGENVECTORS

A central ingredient of the localized reduction framework developed in the main text is the spontaneous localization of Laplacian eigenvectors in heterogeneous networks. In many real-world systems, the eigenmodes of the coupling operator are not spatially extended across the entire network, but instead concentrate around a relatively small subset of nodes. This property allows each mode to be associated with a dominant *host node*, providing a simultaneous mode–node decomposition of the dynamics and enabling reduced descriptions based on sparse local information.

To systematically characterize localization across empirical and synthetic networks, we compute several complementary mode-level localization measures for the Laplacian eigenvectors. Figure 1 shows representative examples of the network families considered throughout this work, including biological, ecological, social, transportation, and random graph models. These networks exhibit markedly different spectral organizations, ranging from highly localized structures to more spatially extended modes.

Let $\boldsymbol{\phi}^{(\alpha)}$ be a normalized eigenvector of the network Laplacian $\mathcal{L}$, satisfying $\sum_{i=1}^{N}\left|\phi_i^{(\alpha)}\right|^2 = 1$. We define the node weight of mode α by

$$w_i^{(\alpha)} = \left|\phi_i^{(\alpha)}\right|^2, \qquad \sum_{i=1}^{N} w_i^{(\alpha)} = 1. \tag{1}$$

The inverse participation ratio is then given by

$$\mathrm{IPR}^{(\alpha)} = \sum_{i=1}^{N}\left(w_i^{(\alpha)}\right)^2 = \sum_{i=1}^{N}\left|\phi_i^{(\alpha)}\right|^4. \tag{2}$$

A larger value of $\mathrm{IPR}^{(\alpha)}$ indicates that the eigenvector mass is concentrated on fewer nodes, while a smaller value corresponds to a more delocalized mode. For comparison across networks of different sizes, we also use the normalized inverse participation ratio

$$\mathrm{IPR}_{\mathrm{norm}}^{(\alpha)} = \frac{\mathrm{IPR}^{(\alpha)} - 1/N}{1 - 1/N}, \tag{3}$$

which maps the fully delocalized case to 0 and the fully localized case to 1.

The effective number of participating nodes is defined as

$$N_{\mathrm{eff}}^{(\alpha)} = \frac{1}{\mathrm{IPR}_{\mathrm{norm}}^{(\alpha)}}. \tag{4}$$

This quantity estimates the number of nodes that effectively support the eigenvector. Therefore, a smaller $N_{\mathrm{eff}}^{(\alpha)}$ indicates stronger localization. However, networks with $N_{\mathrm{eff}}^{(\alpha)} > 100$ tend to produce relatively large approximation errors, which weakens the monotone trend between $N_{\mathrm{eff}}^{(\alpha)}$ and the normalized error.

While the IPR and effective participation number quantify localization globally, the localized reduction itself relies on the existence of dominant host nodes carrying a large fraction of the eigenvector mass. To characterize this feature more directly, we additionally compute peak and tail localization measures.

* masllani@fsu.edu

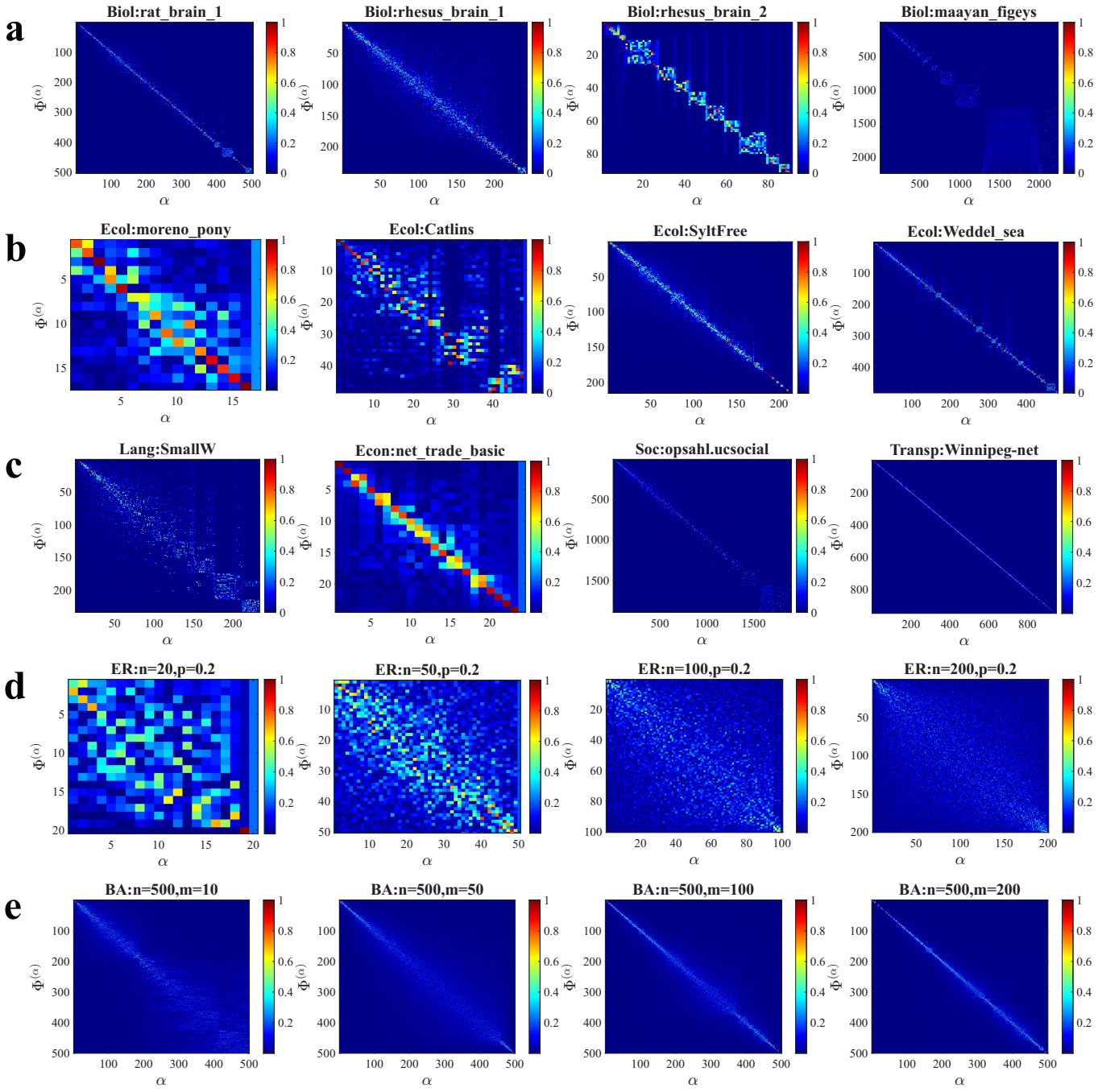

FIG. 1 **Examples of networks from different domains.** (**a**) Biological networks: Mouse's primary visual cortex connectome 1 [1], Connectome of the Rhesus brain, extracted from tract tracing studies collated in the CoCoMac database [2], Connectome of the Rhesus brain, via a retrograde tracer study [3], and the Human protein-protein interactome produced by a mass spectrometry-based approach by Figeys et al. [4]. (**b**) Ecological networks: Dominance among ponies [5], River Foodweb in Caitlins Stream, New Zealand [6], Marine Foodweb in Sylt Tidal Basin, Germany [7], and the Marine Foodweb in Weddel Sea, Antarctica [8]. (**c**) Language network: Citations from papers that cite "Small World Problem" [9]. Economic network: International trade network of manufactured goods [10]. Social network: Online messages from an online community of students from the University of California, Irvine [11]. Transportation network: Roads Network in Winnipeg, Canada [12]. (**d**) Erdős–Rényi random graphs with connection probability $p = 0.2$ and different sizes ($n = 20, 50, 100, 200$). (**e**) Networks generated using the Barabási–Albert model, starting from an initial random graph $G(m_0 = 200, p = 0.1)$, for different attachment parameters $m = 10, 50, 100, 200$.

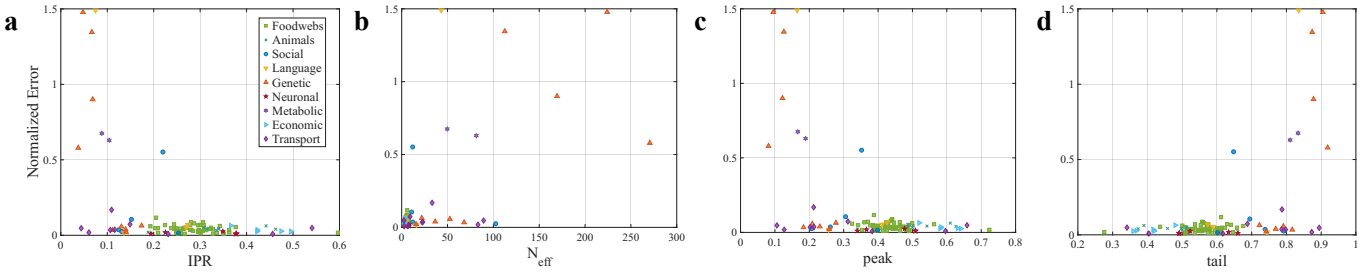

FIG. 2 **Normalized eigenvalue approximation error as a function of different eigenvector localization measures for real-world networks from different domains.** Each point represents one network, with colors and markers indicating the corresponding network category. Panels show the normalized error versus (**a**) the normalized inverse participation ratio (IPR), (**b**) the effective number of participating nodes N_{eff}, (**c**) the peak weight on the dominant node, and (**d**) the tail weight outside the dominant node.

We define the peak weight of the eigenvector by

$$p^{(\alpha)} = \max_{1\le i\le N} w_i^{(\alpha)} = \max_{1\le i\le N} \left|\phi_i^{(\alpha)}\right|^2 . \tag{5}$$

This quantity measures the weight carried by the dominant node of the eigenvector. In our localized mode approximation, the host node of mode α is chosen as

$$\eta(\alpha) = \arg\max_{1\le i\le N} \left|\phi_i^{(\alpha)}\right| .$$

Thus, $p^{(\alpha)}$ directly quantifies how much of the eigenvector is concentrated on the selected host node. Finally, we define the tail weight by

$$\tau^{(\alpha)} = 1 - p^{(\alpha)}. \tag{6}$$

The tail weight measures the total eigenvector mass outside the dominant node. A smaller value of $\tau^{(\alpha)}$ indicates that the mode is more accurately represented by its host node alone. In the numerical results, these quantities are computed for all nontrivial Laplacian eigenvectors, excluding the uniform zero mode, and then averaged over modes to summarize the overall localization strength of each network.

Figure 2 compares the normalized eigenvalue approximation error with four localization measures across real-world networks from different domains. In panel (a), larger IPR values generally correspond to smaller errors, suggesting that stronger eigenvector localization improves the accuracy of the localized approximation. A similar trend is observed in panel (c), where networks with larger peak weights tend to have smaller errors, indicating that modes concentrated on a dominant host node are better captured by the host-node reduction. Panel (d) shows the same effect from the opposite perspective: smaller tail weights, meaning less eigenvector mass outside the dominant node, are associated with smaller approximation errors. Panel (b) shows the relationship with N_{eff}, where smaller values indicate stronger localization. Although smaller N_{eff} is generally expected to reduce the error, several networks with $N_{\text{eff}} > 100$ produce relatively large errors, so this measure does not display as clear a monotone trend as the other localization measures.

II. FURTHER APPLICATIONS

A. Logistic survivability

As a concrete illustration of the localization reduction method for analysing dynamics in heterogeneous empirical systems, we consider the trade network shown in Fig. 3. Despite its modest size, this network already exhibits pronounced Laplacian eigenvector localization, making it a suitable testbed for the framework. To keep the dynamical setting fully transparent, we endow the network with a minimal heterogeneous logistic dynamics [13]

$$\dot{x}_i = r_i x_i(1 - x_i) + D_i \sum_{j=1}^{N} L_{ij} x_j, \quad i = 1, \ldots, N, \tag{7}$$

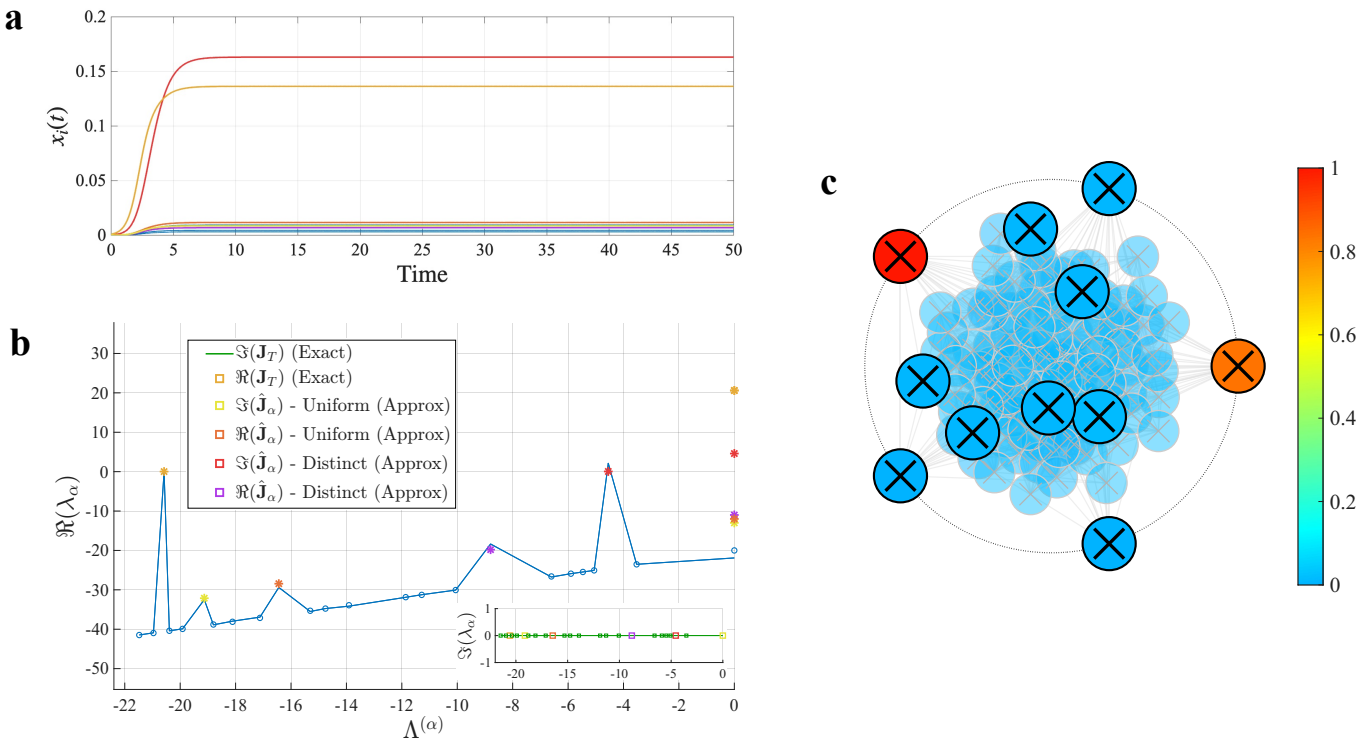

FIG. 3 **Individual dynamics disentanglement in the logistic model.** (**a**) Time series of $x_i(t)$ for a network realization in which all nodes share the same equilibrium point; two trajectories separate from the bulk, consistent with an instability associated with positive real-part eigenvalues. (**b**) Master-stability-style spectrum comparison for the logistic model $\dot{x}_i = r_i x_i(1-x_i)+D\sum_j L_{ij}x_j$ on the trade network. Solid lines denote eigenvalues of the full-system Jacobian $\mathcal{J}_T$, while circles denote the eigenvalues of the localized approximation $\widehat{\mathcal{J}}_\alpha$. The five color-coded modes correspond to five nodes with heterogeneous parameters but identical equilibrium points. Among these, two eigenvalues satisfy $\Re(\lambda) > 0$, indicating linear instability. Here $D = 1$ for all nodes; for the five highlighted nodes, $r = (20.6, -13, -12, -11, 4.6)$, while all remaining nodes have $r = -20$. (**c**) Final-state visualization of $x_i(t)$, where the five outer-ring nodes correspond to the highlighted nodes in panel.

where x_i is a generic node activity (such as production or traded volume), while r_i and D_i are node-dependent growth and coupling parameters. The logistic term captures self-limited local expansion under finite capacity or market saturation, and the Laplacian term describes exchange through network links. The inactive state $x_i^* = 0$ is always an equilibrium. The model is not intended as a literal description of trade dynamics, but as a one-variable prototype that allows the localization reduction method to be demonstrated analytically and interpreted directly at the node level. Linearizing around this reference state yields

$$\dot{\boldsymbol{\xi}} = \mathcal{J}\boldsymbol{\xi}, \qquad \mathcal{J} = \mathrm{diag}(r) + \mathrm{diag}(D)\mathcal{L}, \tag{8}$$

where $\boldsymbol{\xi} = (\xi_1, \ldots, \xi_N)^\top$ is the perturbation vector, $\mathrm{diag}(r) = \mathrm{diag}(r_1, \ldots, r_N)$, and $\mathrm{diag}(D) = \mathrm{diag}(D_1, \ldots, D_N)$. This is the scalar ($M = 1$) counterpart of the general linearized operator of the main text, simplified by the one-variable node dynamics and by the fact that coupling is already written in Laplacian form. The linearized operator is therefore diagonalized by the Laplacian eigenbasis. Each localized mode α inherits the parameters of its host node $\eta(\alpha)$, and the localized Master Stability Function reduces to

$$\Psi\left(\Lambda^{(\alpha)}, \eta(\alpha)\right) := \lambda_{\mathcal{J}}^{(\alpha)} = r_{\eta(\alpha)} + D_{\eta(\alpha)}\Lambda^{(\alpha)}. \tag{9}$$

This approximation provides a direct link between spectral localization and nodewise instability thresholds: instability is controlled not only by parameter values, but also by where the corresponding modes are concentrated in the network.

This mechanism is confirmed in Fig. 3(a,b). The localized MSF in panel (b) predicts that only two modes-nodes acquire positive growth rates, each tied to the nodes on which the corresponding eigenvectors are concentrated. In agreement, the time series in panel (a) show that activity re-emerges almost exclusively on those nodes, while the remainder stay near the inactive state. This contrasts with the collective behavior expected in the homogeneous counterpart of the system, where identical parameters make the uniform mode lose stability first and drive coherent

growth across all nodes. Here, by contrast, competition among heterogeneous local growth rates breaks that global response. Instability no longer unfolds through a purely modal hierarchy, but through a simultaneous mode–node decomposition in which different parts of the network follow distinct routes away from the inactive state. In the trade-network setting, this corresponds to renewed production or expansion of manufactured-goods exchanges arising in selected markets, while much of the system remains dormant.

B. Distributed controlled in information spreading

As a second illustration, we consider a contagion process on a network. In its standard adjacency-based form, the SIS dynamics reads

$$\dot{x}_i = -\gamma x_i + \beta(1 - x_i) \sum_{j=1}^{N} \mathcal{A}_{ij} x_j, \qquad i = 1, \ldots, N, \tag{10}$$

where $x_i(t)$ denotes the activity level at node i, interpreted for instance as infection prevalence, adoption probability, or opinion activation. The parameters γ and β are the recovery and transmission rates, respectively. Linearization about the inactive state $x_i^* = 0$ gives

$$\dot{\boldsymbol{\xi}} = (-\gamma \mathbb{I} + \beta \mathcal{A})\, \boldsymbol{\xi}.$$

If $\mathcal{A}\boldsymbol{\Phi}_{\mathcal{A}}^{(\alpha)} = \Lambda_{\mathcal{A}}^{(\alpha)} \boldsymbol{\Phi}_{\mathcal{A}}^{(\alpha)}$, the corresponding master stability function is

$$\Psi\left(\Lambda_{\mathcal{A}}^{(\alpha)}\right) = -\gamma + \beta \Lambda_{\mathcal{A}}^{(\alpha)}.$$

The resulting spectrum is shown in the inset of Fig. 4(a). Instability is controlled by the leading adjacency eigenmode, so the emerging activity follows a structurally heterogeneous direction. This is confirmed in Fig. 4(b, top), where the steady state closely aligns with the critical eigenvector of $\mathcal{A}$.

In many spreading settings, however, one may instead wish to favour a more homogeneous activation profile. This is naturally relevant not only for epidemics under compensatory interventions, but also for information or opinion dynamics where broad coverage is desirable. To expose such a mechanism, we rewrite the interaction term in Laplacian form $\mathcal{L}$, so that the dynamics becomes

$$\dot{x}_i = -\gamma_i x_i + \beta(1 - x_i) \left(\sum_{j=1}^{N} \mathcal{L}_{ij} x_j + k_i x_i \right), \quad i = 1, \ldots, N, \tag{11}$$

where the recovery rate is now allowed to vary across nodes. Linearizing around the inactive state gives

$$\dot{\boldsymbol{\xi}} = (-\mathrm{diag}(\gamma_i) + \beta\, \mathrm{diag}(k_i) + \beta \mathcal{L})\, \boldsymbol{\xi}.$$

Choosing the node-dependent rates such that $-\gamma_i + \beta k_i = c_i$, the degree dependence is absorbed into a residual diagonal heterogeneity, yielding

$$\dot{\boldsymbol{\xi}} = (\mathrm{diag}(c_i) + \beta \mathcal{L})\, \boldsymbol{\xi}.$$

The system is no longer exactly diagonal in the Laplacian basis, but the localization reduction applies directly: each localized mode inherits the coefficient of its host node. Thus, if $\mathcal{L}\boldsymbol{\Phi}_{\mathcal{L}}^{(\alpha)} = \Lambda_{\mathcal{L}}^{(\alpha)} \boldsymbol{\Phi}_{\mathcal{L}}^{(\alpha)}$, the localized Master Stability Function is

$$\Psi\left(\Lambda_{\mathcal{L}}^{(\alpha)}, \eta(\alpha)\right) = c_{\eta(\alpha)} + \beta \Lambda_{\mathcal{L}}^{(\alpha)}. \tag{12}$$

For the illustrative realization shown in Fig. 4, we choose the special case $c_i \equiv c$, so that the localized expression coincides with the exact Laplacian spectrum. The corresponding spectrum is reported in Fig. 4(a, main panel). The dominant mode is now the Laplacian eigenvector associated with $\Lambda_{\mathcal{L}}^{(c)} = 0$, namely the uniform direction $\mathbf{1} = (1, \ldots, 1)^T$ for a connected network. The onset of spreading therefore aligns with a collective mode that is spatially homogeneous, rather than with a structurally localized adjacency eigenvector. Accordingly, Fig. 4(b, bottom) shows an approximately uniform steady-state profile. In this way, degree-dependent recovery rates provide a simple mechanism through which heterogeneous networks can be steered from localized outbreaks toward approximately uniform contagion or adoption patterns.

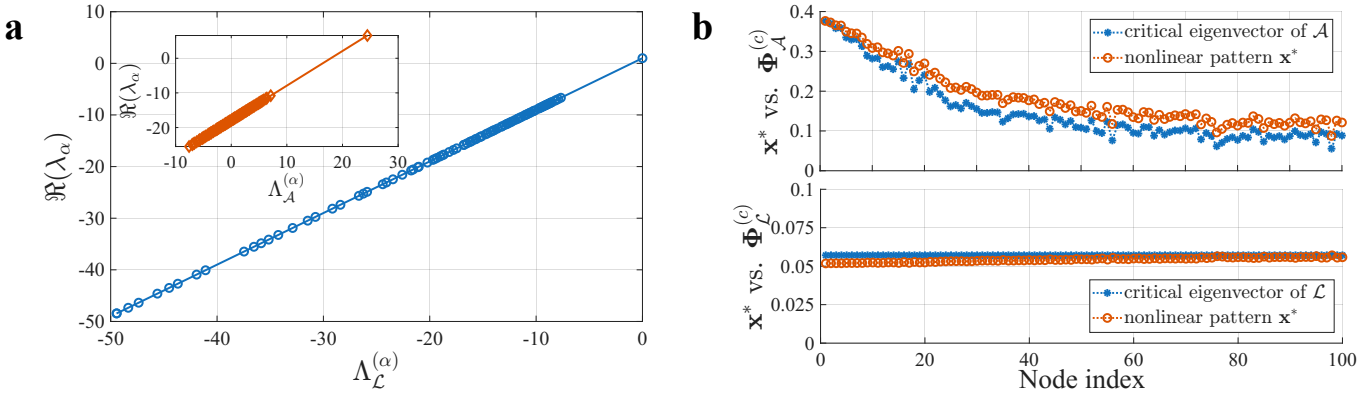

FIG. 4 **Comparison between adjacency-based and Laplacian-based contagion dynamics.** (**a**) Master stability spectra for the two formulations. The inset shows the adjacency-based case, where growth rates are controlled by the eigenvalues of $\mathcal{A}$. The main panel shows the Laplacian-based case, where the spectrum is organized by the eigenvalues of $\mathcal{L}$. (**b**) Steady-state activity profile x^* compared with the dominant mode in each formulation. Top: x_i^* against the critical eigenvector of $\mathcal{A}$, showing a heterogeneous pattern concentrated on structurally favoured nodes. Bottom: x_i^* against the critical eigenvector of $\mathcal{L}$, showing an approximately uniform activation profile aligned with the collective Laplacian mode.

III. BEYOND MODEL CONSTRAINT

The localized reduction framework developed in the main text does not rely on a specific reaction–diffusion model, but rather on the spectral organization of the coupling operator and the localization properties of the corresponding Laplacian eigenvectors. To illustrate this robustness beyond identical node dynamics, we consider a heterogeneous network composed of two distinct reaction–diffusion systems coupled through the same Laplacian structure. In particular, we combine Brusselator and Mimura–Murray nodes within a single network and investigate whether the same classes of collective patterns persist under mixed local kinetics.

The Mimura–Murray model was introduced as a minimal predator–prey reaction system capable of exhibiting oscillatory dynamics through nonlinear species interactions [14]. In its aspatial form, the local kinetics of the prey density ϕ and predator density ψ is governed by

$$\dot{\phi} = \phi\left(\frac{a + b\phi - \phi^2}{c} - \psi\right), \qquad \dot{\psi} = \psi\big(\phi - (1 + d\psi)\big), \tag{13}$$

with all parameters positive. Besides trivial equilibria, the system admits a positive steady state

$$\phi^* = \frac{(bd - c) + \sqrt{(bd - c)^2 + 4d(c + ad)}}{2d}, \qquad \psi^* = \frac{\phi^* - 1}{d}. \tag{14}$$

Linear stability analysis shows that this equilibrium loses stability through a Hopf bifurcation when the trace of the Jacobian vanishes while the determinant remains positive. This condition yields the critical threshold $c_H = \phi^*(b - 2\phi^*)/d\psi^*$. Beyond this threshold the system develops stable limit-cycle oscillations.

We partition the network into two subpopulations governed by distinct local kinetics but coupled through the same Laplacian L. The first group follows the Brusselator model with state $(u_i^{\mathrm{B}}, v_i^{\mathrm{B}})$, parameters $(a^{\mathrm{B}}, b^{\mathrm{B}}, c^{\mathrm{B}}, d^{\mathrm{B}})$, and diffusion $(D_u^{\mathrm{B}}, D_v^{\mathrm{B}})$ (constant across the Brusselator group). The second group follows the *Mimura–Murray (MM)* model with state $(u_i^{\mathrm{M}}, v_i^{\mathrm{M}})$, parameters $(a^{\mathrm{M}}, b^{\mathrm{M}}, c^{\mathrm{M}}, d^{\mathrm{M}})$, and diffusion $(D_u^{\mathrm{M}}, D_v^{\mathrm{M}})$ (constant across the MM group).

The Brusselator model is given by:

$$\dot{u}_i^{\mathrm{B}} = a^{\mathrm{B}} - (b^{\mathrm{B}} + d^{\mathrm{B}})u_i^{\mathrm{B}} + c^{\mathrm{B}}(u_i^{\mathrm{B}})^2 v_i^{\mathrm{B}} + D_u^{\mathrm{B}} \sum_{j=1}^{N} L_{ij} u_j^{\mathrm{B}}, \tag{15}$$

$$\dot{v}_i^{\mathrm{B}} = b^{\mathrm{B}} u_i^{\mathrm{B}} - c^{\mathrm{B}}(u_i^{\mathrm{B}})^2 v_i^{\mathrm{B}} + D_v^{\mathrm{B}} \sum_{j=1}^{N} L_{ij} v_j^{\mathrm{B}}. \tag{16}$$

The aspatial equilibrium is $u_{\mathrm{B}}^* = a^{\mathrm{B}}/d^{\mathrm{B}}$, $v_{\mathrm{B}}^* = b^{\mathrm{B}} d^{\mathrm{B}}/a^{\mathrm{B}} c^{\mathrm{B}}$.

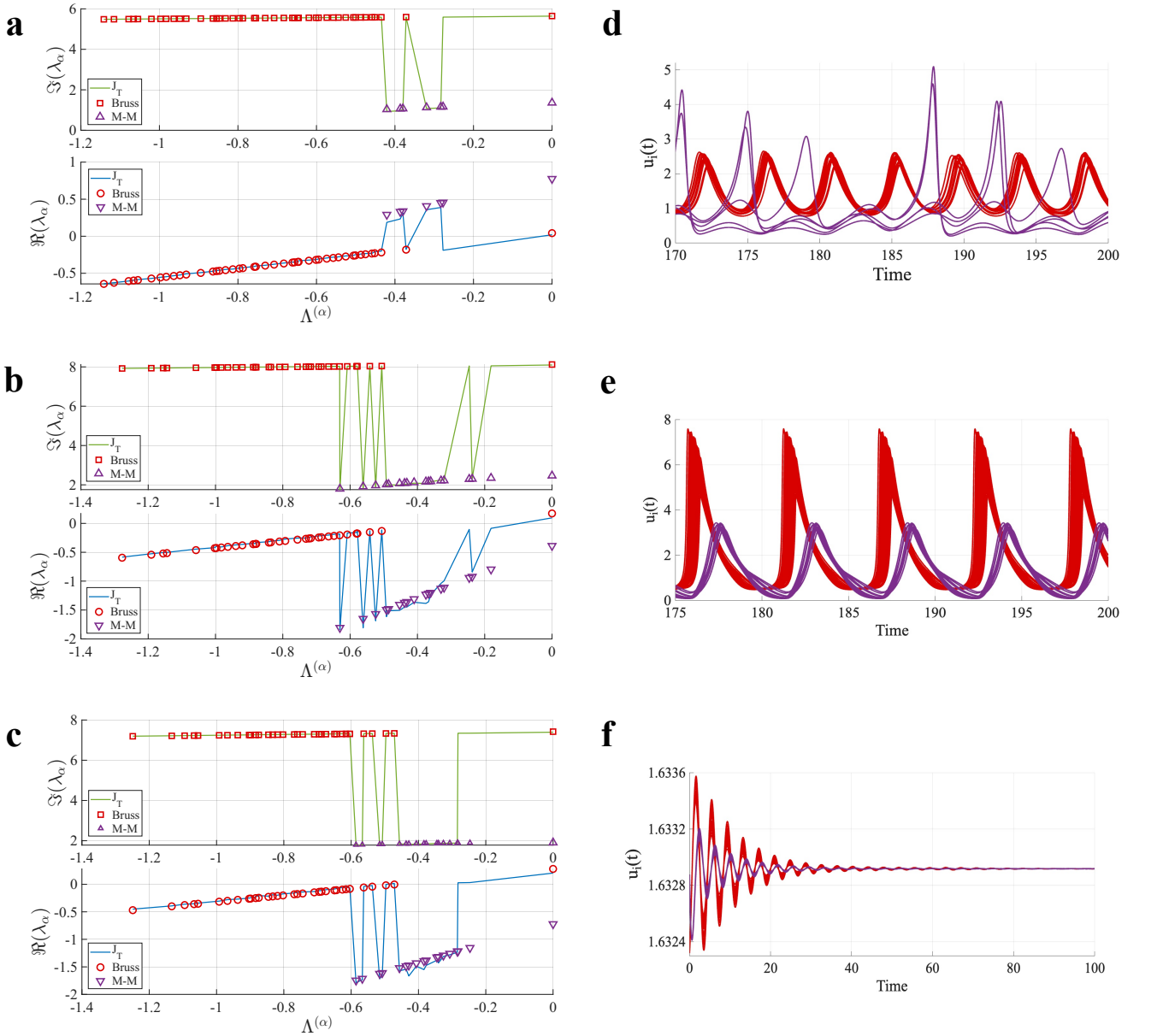

FIG. 5 **Dynamics of mixed reaction–diffusion models on the same network.** Red quantities correspond to the Brusselator model, while purple quantities correspond to the Mimura–Murray model. Panels (**a**)–(**c**) show the Master Stability Function together with the eigenvalues of the exact Jacobian $\mathcal{J}_T$ and the localized reduced operator $\widehat{\mathcal{J}}_\alpha$, illustrating the agreement between the full spectral dynamics and the localization-based approximation. Panels (**d**)–(**f**) display the corresponding node dynamics $u_i(t)$ associated with the unstable modes. (**a**,**d**) Chaotic chimera, characterized by coexistence of coherent and irregular oscillatory regions; (**b**,**e**) cluster synchronization, where groups of nodes evolve coherently; and (**c**,**f**) oscillation death, corresponding to stationary heterogeneous states emerging from the localized instability structure.

Mimura–Murray model:

$$\dot{u}_i^{\mathrm{M}} = u_i^{\mathrm{M}}\left(\frac{a^{\mathrm{M}} + b^{\mathrm{M}}u_i^{\mathrm{M}} - (u_i^{\mathrm{M}})^2}{c^{\mathrm{M}}} - v_i^{\mathrm{M}}\right) + D_u^{\mathrm{M}}\sum_{j=1}^{N} L_{ij}u_j^{\mathrm{M}}, \tag{17}$$

$$\dot{v}_i^{\mathrm{M}} = v_i^{\mathrm{M}}\Big(u_i^{\mathrm{M}} - (1 + d^{\mathrm{M}}v_i^{\mathrm{M}})\Big) + D_v^{\mathrm{M}}\sum_{j=1}^{N} L_{ij}v_j^{\mathrm{M}}. \tag{18}$$

TABLE I Parameter sets grouped by node classes (all values rounded to 4 decimals). Distinct parameter tuples define distinct groups.

Case / Group	a	b	c	d	D_u	D_v
Two Model: Cluster						
Brusselator (35 nodes)	11.3964	18.0104	2.7221	5.3598	0.5000	0.7000
Mimura–Murray (15 nodes)	3.9746	4.7571	3.0751	0.3620	0.5000	4.0000
Two Model: Oscillation Death						
Brusselator (35 nodes)	6.8825	17.8565	4.9064	4.2149	0.5000	0.7000
Mimura–Murray (15 nodes)	4.8332	2.0397	2.4666	0.2840	0.5000	3.0000
Two Model: Chaotic						
Brusselator (45 nodes)	6.1659	11.9815	3.4161	4.0742	0.5000	0.7000
Mimura–Murray (5 nodes)	0.7816	19.5058	12.0864	0.2215	0.5000	1.8000

Its positive aspatial equilibrium satisfies

$$u_{\mathrm{M}}^{*} = \frac{(b^{\mathrm{M}}d^{\mathrm{M}} - c^{\mathrm{M}}) + \sqrt{(b^{\mathrm{M}}d^{\mathrm{M}} - c^{\mathrm{M}})^2 + 4d^{\mathrm{M}}(c^{\mathrm{M}} + a^{\mathrm{M}}d^{\mathrm{M}})}}{2d^{\mathrm{M}}}, \qquad v_{\mathrm{M}}^{*} = \frac{u_{\mathrm{M}}^{*} - 1}{d^{\mathrm{M}}}. \tag{19}$$

We first fix a single MM parameter set $(a^{\mathrm{M}}, b^{\mathrm{M}}, c^{\mathrm{M}}, d^{\mathrm{M}})$ and compute its equilibrium $(u_{\mathrm{M}}^{*}, v_{\mathrm{M}}^{*})$ from the formulas above. We then choose the Brusselator parameters so that the Brusselator equilibrium equals the same pair: pick any $c^{\mathrm{B}} > 0$ and $d^{\mathrm{B}} > 0$, and set $a^{\mathrm{B}} = u_{\mathrm{M}}^{*}\, d^{\mathrm{B}}$, $b^{\mathrm{B}} = u_{\mathrm{M}}^{*}\, c^{\mathrm{B}}\, v_{\mathrm{M}}^{*}$, which enforces, identically, $u_{\mathrm{B}}^{*} = a^{\mathrm{B}}/d^{\mathrm{B}} = u_{\mathrm{M}}^{*}$, $v_{\mathrm{B}}^{*} = b^{\mathrm{B}}d^{\mathrm{B}}/a^{\mathrm{B}}c^{\mathrm{B}} = v_{\mathrm{M}}^{*}$. (Here diffusion pairs $(D_u^{\mathrm{B}}, D_v^{\mathrm{B}})$ and $(D_u^{\mathrm{M}}, D_v^{\mathrm{M}})$ are model-specific and remain independent; typically $D_u \neq D_v$.)

Figure 5 shows the resulting dynamics for the mixed-model network. Despite the coexistence of two fundamentally different local reaction mechanisms, the collective behavior remains strongly organized by the Laplacian spectral structure. Panels (a)–(c) compare the eigenvalues of the full Jacobian $\mathcal{J}_T$ with the reduced localized approximation $\widehat{\mathcal{J}}_\alpha$, while panels (d)–(f) display the corresponding node dynamics. The system exhibits chaotic chimera states, cluster synchronization, and oscillation death, demonstrating that the localization-based reduction remains effective even when the node dynamics are heterogeneous and model-dependent.

These results show that the emergence of collective patterns is governed primarily by the Laplacian modes and their localization properties rather than by the precise form of the local kinetics. In particular, near instability onset, the nonlinear dynamics inherit the spatial organization of the critical localized eigenvectors, allowing the localized reduction framework to remain predictive even beyond identical-model constraints.

IV. IDENTICAL HOPF CONDITIONS, DIFFERENT LIMIT CYCLES

To demonstrate that the same equilibrium point does not uniquely determine the nonlinear oscillatory dynamics, we consider two uncoupled single-node Brusselator systems with different parameter sets chosen to share the same steady state $u^* = a/d$, $v^* = bd/ac$. We first generate one admissible parameter set (a_1, b_1, c_1, d_1), and then construct a second set $(a_2, b_2, c_2, d_2) \neq (a_1, b_1, c_1, d_1)$ under the constraints

$$\frac{a_1}{d_1} = \frac{a_2}{d_2}, \qquad \frac{b_1 d_1}{a_1 c_1} = \frac{b_2 d_2}{a_2 c_2},$$

so that both systems have the same equilibrium point. In the example shown here, the two parameter sets are $(a, b, c, d) = (1.2955, 8.2066, 4.9526, 4.3203)$ and $(a, b, c, d) = (1.9522, 9.9884, 6.0280, 6.5102)$, which yield the common equilibrium $(u^*, v^*) \approx (0.2999, 5.5260)$. We then simulate the corresponding single-node dynamics and compare the resulting trajectories $u(t)$.

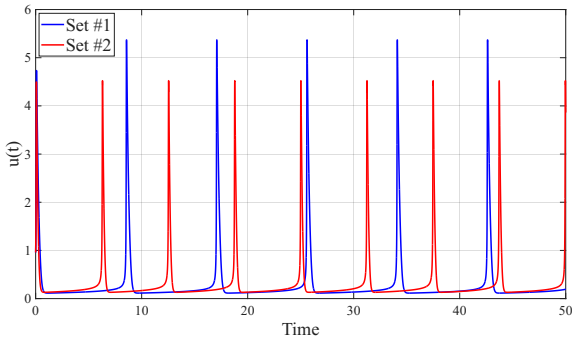

FIG. 6 **Time series $u(t)$ of two single-node Brusselator systems with identical equilibrium points but different parameter values.** The parameter set for Node 1 is $(a, b, c, d) = (1.2955, 8.2066, 4.9526, 4.3203)$, and the parameter set for Node 2 is $(a, b, c, d) = (1.9522, 9.9884, 6.0280, 6.5102)$.

However, the simulated time series $u(t)$ reveal different limit cycles for the two nodes. This confirms that even when the fixed point is preserved, differences in the underlying kinetic parameters remain sufficient to alter the nonlinear periodic dynamics, so the equilibrium location alone is not enough to characterize the full behavior of the system.

V. EXOTIC PATTERNS PARAMATERS

The parameter sets reported in Table II correspond to the dynamical regimes shown in Fig. 3 of the main text. Distinct parameter tuples therefore define distinct localized node groups responsible for shaping the observed collective dynamics, including cluster synchronization, amplitude chimera, amplitude–phase chimera, and oscillon patterns.

TABLE II Parameter sets grouped by node classes (all values rounded to 4 decimals). Distinct parameter tuples define distinct groups.

Set	N	a	b	c	d	D_u	D_v
Cluster sync							
1	495	4.4171	5.0403	0.7074	3.0175	0.5000	1.0000
2	1	0.0764	3.7791	0.5304	0.0522	0.4811	1.1545
3	1	0.0764	3.7791	0.5304	0.0522	0.5235	1.2563
4	1	0.0764	3.7791	0.5304	0.0522	0.5000	1.2000
5	1	0.0764	3.7791	0.5304	0.0522	0.8693	2.0863
6	1	0.0764	3.7791	0.5304	0.0522	1.0606	2.5454
Amplitude chimera							
1	495	2.8400	5.6603	2.2308	2.5675	0.5000	1.0000
2	1	0.8259	4.8367	1.9062	0.7467	0.5000	1.1000
3	1	1.8503	8.2902	3.2673	1.6727	0.5000	1.1000
4	1	0.0402	3.9411	1.5533	0.0364	0.5000	1.1000
5	1	0.7818	4.8592	1.9151	0.7068	0.5000	1.1000
6	1	0.2508	4.8161	1.8981	0.2267	0.5000	1.1000
Amplitude –phase chimera							
1	97	3.3681	3.7531	0.6336	2.2732	0.5000	1.5000
2	1	2.1504	5.5862	0.9477	1.4513	0.5000	0.7000
3	1	1.7703	5.0383	0.8547	1.1948	0.5000	0.7000
4	1	2.2043	4.3802	0.7431	1.4877	0.5000	0.7000
Oscillon pattern							
1	93	1.5718	5.3368	2.9803	5.3213	0.5000	2.0000
2	1	52.6674	191.5065	106.9453	178.3106	0.5000	2.0000
3	1	17.7655	66.2388	36.9905	60.1468	0.5000	2.0000
4	1	50.2845	181.7927	101.5207	170.2429	0.5000	2.0000
5	1	14.5962	54.8355	30.6225	49.4170	0.5000	2.0000
6	1	42.9098	158.1963	88.3435	145.2753	0.5000	2.0000
7	1	16.5602	62.0546	34.6539	56.0663	0.5000	2.0000
8	1	1.5718	5.3368	2.9803	5.3213	0.5000	2.0000

VI. EIGENVALUE PAIRING ALGORITHM

The eigenvalues of the reduced Jacobians $\widehat{\mathcal{J}}_\alpha$ associated with the transversal Laplacian modes $\Lambda^{(\alpha)}$ are naturally indexed by the mode label $\alpha \geq 2$, with each mode contributing M eigenvalues. By contrast, the MN eigenvalues of the full system Jacobian $\mathcal{J}_T \in \mathbb{C}^{MN\times MN}$ are not canonically organized according to Laplacian modes. To compare the reduced and full spectra, we construct two sets, $\mathcal{U}$, obtained by aggregating the eigenvalues of $\{\widehat{\mathcal{J}}_\alpha\}_{\alpha=2}^{N}$, and $\mathcal{V}$, containing the eigenvalues of $\mathcal{J}_T$. Because there is no natural ordering aligning the two spectra, we determine an injective correspondence by solving a minimum-weight bipartite matching problem in the complex plane, where the pairing cost is the complex modulus of the eigenvalue difference. The optimal assignment, computed using the Hungarian algorithm [15, 16], minimizes the total spectral discrepancy between the reduced and full systems. With the resulting pairing between $\mathcal{U}$ and a subset of $\mathcal{V}$, we quantify agreement via the mean normalized error, defined as the average complex distance between matched eigenvalues, normalized by their magnitude (with a unit lower bound to ensure robustness near zero). This metric provides a systematic measure of how accurately the localized transversal approximation reproduces the full Jacobian spectrum.

VII. EMPIRICAL NETWORKS DATA ANALYSIS

Table III summarizes the empirical networks used throughout this work together with the localization indicators introduced in Sec. I. For each network we report the number of nodes and edges, the inverse participation ratio (IPR), effective participation number N_{eff}, peak weight, tail weight, and the normalized approximation error associated with the localized spectral reduction.

TABLE III: Summary of Networks Grouped by Domain

Network Name	Nodes	Edges	IPR	N_{eff}	Peak	Tail	NormErr	Ref
Social								
Political Blogs Network	1224	16664	0.2540	7.0499	0.3981	0.6019	0.0145	[17]
E-mail network for the Democratic National Convention	1891	4465	0.1435	91.8896	0.2072	0.7928	0.0251	[18]
Friendship among college students in a course about leadership	32	80	0.1521	7.5996	0.3054	0.6946	0.1052	[19]
Friendship among highschool students	70	274	0.1246	9.9463	0.2611	0.7389	0.0364	[20]
Online messages from an online community of students from the University of California, Irvine	1899	13838	0.2205	11.8227	0.3520	0.6480	0.5517	[11]
Transport								
London tube network	270	317	0.1066	19.3557	0.2021	0.7979	0.0348	[21]
Flights between airports in the United States	1574	17215	0.5411	2.4696	0.6587	0.3413	0.0364	[22]
Paris metropolitan train grid	302	359	0.1162	20.1148	0.2136	0.7864	0.5789	[21]
Roads Network in Rome, Italy	3353	4831	0.1093	31.2016	0.2128	0.7872	0.0570	[23]
London bike-sharing network	750	120578	0.2311	6.7565	0.3829	0.6171	0.9004	[24]
Roads Network in Sioux Falls, USA	24	38	0.1490	6.3817	0.3122	0.6878	0.6752	[25]
Roads Network in Barcelona, Spain	930	1798	0.0604	71.3879	0.1270	0.8730	0.0284	[12]
Roads Network in Winnipeg, Canada	949	1823	0.4562	2.7037	0.5958	0.4042	0.0719	[12]
Roads Network in Terrassa, Spain	1603	2320	0.0438	80.1071	0.1056	0.8944	1.3457	[12]
Language								
Word adjacency network for Dr. Seuss's Green Eggs and Ham book	50	93	0.2737	4.7556	0.4261	0.5739	0.0668	[20]
Citation network of the journal Scientometrics	2729	10400	0.0749	42.0302	0.1647	0.8353	0.0492	[26]
Citations to Small, Griffith and descendants	1024	4917	0.1360	15.6264	0.2561	0.7439	0.0122	[27]
Citations from papers that cite "Small World Problem"	233	994	0.2697	6.0617	0.4115	0.5885	0.0529	[9]
Economic								
International trade network of manufactured goods	24	195	0.4956	2.2696	0.6408	0.3592	0.0253	[10]
International trade network of crude animal and vegetable material	24	195	0.4746	2.3609	0.6314	0.3686	0.0275	[10]
International trade network of diplomatic exchanges	24	199	0.4232	2.6334	0.5834	0.4166	0.0357	[10]
International trade network of manufactured food products	24	201	0.4227	2.8654	0.5806	0.4194	0.0254	[10]
International trade network of minerals	24	97	0.3662	3.4501	0.5197	0.4803	0.0642	[10]

Network Name	Nodes	Edges	IPR	N_{eff}	Peak	Tail	NormErr	Ref
Ecological								
Marine Foodweb in Bahia Falsa, Mexico	166	7707	0.2522	6.3471	0.3936	0.6064	0.0095	[7]
Marine Foodweb in Benguela Current, South Africa	29	198	0.3079	4.1707	0.4680	0.5320	0.0386	[28]
River Foodweb in Berwick Stream, New Zealand	77	240	0.2642	5.0184	0.4216	0.5784	0.0418	[6]
River Foodweb in Black Rock Stream, New Zealand	86	375	0.2441	5.1924	0.3933	0.6067	0.0449	[29]
Lake Foodweb in Bridge Broom Lake	25	106	0.3763	2.9757	0.5631	0.4369	0.0540	[30]
River Foodweb in Broad Stream, New Zealand	94	565	0.2787	4.7003	0.4244	0.5756	0.0691	[29]
Terrestrial Foodweb in Scotch Broom, England	86	224	0.3047	4.2344	0.4465	0.5535	0.0660	[31]
Fossil Assemblage Foodweb from Burgess Shale, Canada	48	247	0.3234	3.8215	0.4904	0.5096	0.0505	[32]
River Foodweb in Canton Creek, New Zealand	102	697	0.2569	6.0467	0.3996	0.6004	0.0445	[29]
Marine Foodweb in Carpinteria Salt Marsh Reserve, USA	166	6557	0.2582	6.5232	0.4005	0.5995	0.0138	[7]
River Foodweb in Caitlins Stream, New Zealand	48	110	0.3422	3.9402	0.4993	0.5007	0.0619	[33]
Marine Foodweb in Cayman Islands	242	3766	0.2096	7.4436	0.3528	0.6472	0.0167	[34]
Fossil Assemblage Foodweb from Chengjiang Shale, China	33	88	0.2802	4.4061	0.4416	0.5584	0.0870	[32]
Marine Foodweb in Chesapeake Bay, USA	31	68	0.2052	5.1233	0.3879	0.6121	0.1171	[35]
River Foodweb in Coweeta, USA	71	148	0.2956	4.8305	0.4295	0.5705	0.0659	[6]
River Foodweb in Coweeta, USA	58	126	0.2870	4.6837	0.4368	0.5632	0.0789	[6]
River Foodweb in Dempsters Stream during autumn, New Zealand	83	415	0.2490	5.2384	0.3853	0.6147	0.0450	[33]
River Foodweb in Dempsters Stream during spring, New Zealand	93	538	0.2782	5.2245	0.4191	0.5809	0.0347	[33]
River Foodweb in Dempsters Stream during summer, New Zealand	107	966	0.2493	5.6925	0.4054	0.5946	0.0299	[29]
Terrestrial Foodweb in El Verde Field Station, Puerto Rico	155	1440	0.2951	4.9220	0.4421	0.5579	0.0239	[20]
Marine Foodweb in Estero de Punta Banda, Mexico	143	3412	0.2483	6.2012	0.3889	0.6111	0.0169	[7]
Marine Foodweb in Flensburg Fjord, Germany/Denmark	77	578	0.3196	4.3824	0.4631	0.5369	0.0424	[7]
Marine Foodweb in Florida Bay during dry season	128	2106	0.5967	1.9643	0.7240	0.2760	0.0179	[36]
River Foodweb in German Creek, New Zealand	84	353	0.2378	5.5507	0.3858	0.6142	0.0477	[29]
Terrestrial Foodweb in grasslands of the United Kingdom	61	97	0.3065	5.2085	0.4404	0.5596	0.0856	[20]
River Foodweb in Healy Creek, New Zealand	96	634	0.2552	5.4068	0.3960	0.6040	0.0254	[29]
River Foodweb in Kye Burn, New Zealand	98	629	0.3023	4.4838	0.4514	0.5486	0.0257	[29]
River Foodweb in Little Kye Burn, New Zealand	78	375	0.2093	6.1651	0.3423	0.6577	0.0480	[29]
Lake Foodweb in Little Rock Lake, USA	183	2452	0.3630	5.0607	0.4820	0.5180	0.0187	[37]
Lake Foodweb in Lough Hyne, Ireland	349	5102	0.2549	6.1405	0.3884	0.6116	0.0348	[8]
River Foodweb in Martins Stream, USA	105	343	0.1931	7.2013	0.3240	0.6760	0.0589	[6]
Dominance among ants	16	36	0.4419	2.5799	0.6100	0.3900	0.0103	[38]
Dominance among bisons	26	222	0.3396	3.4525	0.5025	0.4975	0.0621	[39]
Dominance among cattle	28	205	0.3153	4.1664	0.4882	0.5118	0.0431	[40]
Dominance among kangaroos	17	91	0.4626	2.2851	0.6268	0.3732	0.0427	[41]
Dominance among macaques	62	1167	0.1881	7.2149	0.3397	0.6603	0.0403	[42]
Dominance among ponies	17	129	0.3402	3.0667	0.5422	0.4578	0.0208	[5]
Dominance among sheep	28	235	0.3352	4.0321	0.5004	0.4996	0.0423	[43]
Dominance among wolves	16	111	0.3078	3.6259	0.4864	0.5136	0.0326	[44]
River Foodweb in Narrowdale Stream, New Zealand	71	155	0.2439	6.3379	0.3708	0.6292	0.0522	[45]
River Foodweb in North Col Stream, New Zealand	78	241	0.3275	4.2632	0.4765	0.5235	0.0720	[45]
Marine Foodweb in Otago Harbour, New Zealand	215	11648	0.3504	4.4017	0.4906	0.5094	1.4781	[7]
River Foodweb in Powder Stream, New Zealand	78	268	0.2996	4.0370	0.4630	0.5370	0.0216	[6]
Marine Foodweb in Northeast United States Shelf	79	1396	0.3357	3.8972	0.4911	0.5089	0.0636	[46]
Lake Foodweb in Skipwith Common, England	25	193	0.3052	3.9209	0.4844	0.5156	0.0337	[47]
Marine Foodweb in St. Marks Estuary, US	48	221	0.2036	5.5735	0.3774	0.6226	0.0395	[48]
Terrestrial Foodweb in Saint-Martin Island, Lesser Antilles	42	205	0.2846	5.9639	0.4331	0.5669	0.0480	[49]
River Foodweb in Stony Stream, New Zealand	109	829	0.2974	4.7504	0.4472	0.5528	0.1687	[29]
River Foodweb in Stony Stream, New Zealand	112	832	0.2958	4.7437	0.4439	0.5561	1.4906	[29]

Network Name	Nodes	Edges	IPR	N_{eff}	Peak	Tail	NormErr	Ref
River Foodweb in Sutton Stream during autumn, New Zealand	80	335	0.2702	4.5114	0.4183	0.5817	0.0157	[33]
River Foodweb in Sutton Stream during spring, New Zealand	74	391	0.3133	4.5380	0.4531	0.5469	0.0284	[33]
River Foodweb in Sutton Stream during summer, New Zealand	87	424	0.3621	3.7374	0.4810	0.5190	0.0173	[29]
Marine Foodweb in Sylt Tidal Basin, Germany	215	11567	0.3278	4.7449	0.4640	0.5360	0.0529	[7]
River Foodweb in Troy Stream, USA	77	181	0.2245	5.8638	0.3600	0.6400	0.0464	[6]
River Foodweb in Venlaw Stream, New Zealand	66	187	0.2652	4.8426	0.4269	0.5731	0.0297	[6]
Marine Foodweb in Weddel Sea, Antarctica	483	15062	0.3009	5.2063	0.4259	0.5741	0.0356	[8]
Marine Foodweb in Ythan Estuary, Scotland	82	394	0.2807	4.6295	0.4340	0.5660	0.0298	[50]
Marine Foodweb in Ythan Estuary, Scotland	166	7275	0.2665	5.7474	0.4138	0.5862	0.0511	[7]
Biological								
Human protein-protein interactome produced by a mass spectrometry-based approach by Figeys et al.	2239	6432	0.1045	74.4869	0.1891	0.8109	0.0090	[4]
Neuronal network for a mouse brain	213	16242	0.1940	7.5993	0.3398	0.6602	0.0365	[20]
Human gene regulatory network for a person with cancer	4049	11706	0.0477	202.2597	0.0952	0.9048	0.0693	[51]
Neuronal network for Caenorhabditis elegans	297	2148	0.1405	14.6583	0.2581	0.7419	0.0090	[52]
Gene regulatory network for Escherichia coli from Thieffry et al.	418	519	0.1599	19.4156	0.2774	0.7226	0.0092	[53]
Gene regulatory network for Escherichia coli from Salgado et al.	1470	2902	0.1134	62.0735	0.1832	0.8168	0.0117	[54]
Gene regulatory network for Mycobacterium tuberculosis	1624	3163	0.0712	99.6479	0.1260	0.8740	0.0187	[55]
Human gene regulatory network for a healthy person	4071	8465	0.0375	240.1826	0.0813	0.9187	0.0251	[51]
Gene regulatory network for Pseudomonas aeruginosa	691	984	0.1286	45.9039	0.2089	0.7911	0.0731	[56]
Gene regulatory network for Saccharomyces cerevisiae from Harbison et al.	2933	6150	0.0696	152.1040	0.1220	0.8780	0.0184	[57]
Metabolic network for Saccharomyces cerevisiae	1510	3807	0.0883	46.8165	0.1663	0.8337	0.0086	[58]
Gene regulatory network for Saccharomyces cerevisiae from Constanzo et al.	688	1078	0.1360	32.8261	0.2307	0.7693	0.0086	[59]
Connectome of the Rhesus brain, extracted from tract tracing studies collated in the CoCoMac database	242	3054	0.2252	7.4285	0.3662	0.6338	0.0154	[2]
Connectome of the Rhesus brain, via a retrograde tracer study	91	582	0.3490	4.0950	0.4772	0.5228	0.0365	[3]
Mouse's primary visual cortex connectome 1	503	23030	0.3783	4.2415	0.5085	0.4915	0.0691	[1]
Mouse's primary visual cortex connectome 2	502	24656	0.3764	4.0911	0.5090	0.4910	0.0095	[60]
Mouse's primary visual cortex connectome 3	493	25988	0.3782	4.0854	0.5084	0.4916	0.0107	[61]

[1] M. Bota and L. W. Swanson, J. Comp. Neurol. **500**, 807 (2007).
[2] L. Harriger, M. P. V. D. Heuvel, and O. Sporns, PLoS ONE **7**, e46497 (2012).
[3] N. T. Markov, M. Ercsey-Ravasz, C. Lamy, A. R. R. Gomes, L. Magrou, P. Misery, P. Giroud, P. Barone, C. Dehay, Z. Toroczkai, *et al.*, Proc. Natl. Acad. Sci. USA **110**, 5187 (2013).
[4] R. M. Ewing, P. Chu, F. Elisma, H. Li, P. Taylor, S. Climie, L. McBroom-Cerajewski, M. D. Robinson, L. O'Connor, M. Li, *et al.*, Mol. Syst. Biol. **3**, 89 (2007).
[5] T. Clutton-Brock, P. Greenwood, and R. Powell, Z. Tierpsychol. **41**, 202 (1976).
[6] R. M. Thompson and C. Townsend, Ecology **84**, 145 (2003).
[7] J. A. Dunne, K. D. Lafferty, A. P. Dobson, R. F. Hechinger, A. M. Kuris, N. D. Martinez, J. P. McLaughlin, K. N. Mouritsen, R. Poulin, K. Reise, *et al.*, PLoS Biol. **11**, e1001579 (2013).
[8] A. Eklöf, U. Jacob, J. Kopp, J. Bosch, R. Castro-Urgal, N. P. Chacoff, B. Dalsgaard, C. de Sassi, M. Galetti, P. R. Guimarães, *et al.*, Ecol. Lett. **16**, 577 (2013).

[9] E. Garfield, Index of citation networks produced by analyses from the software histcite, http://www.garfield.library.upenn.edu/histcomp/index.html.
[10] W. de Nooy, A. Mrvar, and V. Batagelj, *Exploratory Social Network Analysis with Pajek*, Structural Analysis in the Social Sciences (Cambridge University Press, 2011).
[11] T. Opsahl and P. Panzarasa, Social Networks **31**, 155 (2009).
[12] Transportation Networks for Research Core Team, Transportation networks for research, https://github.com/bstabler/TransportationNetworks.
[13] J. D. Murray, *Mathematical biology*, 3rd ed., Interdisciplinary applied mathematics (Springer, New York, 2002).
[14] M. Mimura and J. Murray, Journal of Theoretical Biology **75**, 249 (1978).
[15] H. W. Kuhn, Naval research logistics quarterly **2**, 83 (1955).
[16] J. Munkres, Journal of the society for industrial and applied mathematics **5**, 32 (1957).
[17] L. A. Adamic and N. Glance, *The Political Blogosphere and the 2004 U.S. Election: Divided They Blog* (ACM Press, New York, NY, 2005).
[18] J. Kunegis, Dnc emails co-recipients, kONECT, the Koblenz Network Collection (2016), https://networks.skewed.de/net/dnc.
[19] R. Milo, S. Itzkovitz, N. Kashtan, R. Levitt, S. Shen-Orr, I. Ayzenshtat, M. Sheffer, and U. Alon, Science **303**, 1538 (2004).
[20] S. Johnson, Network data repository from various sources, https://www.samuel-johnson.org/data.
[21] M. J. Williams and M. Musolesi, Royal Society Open Science **3**, 160196 (2016).
[22] T. Opsahl, F. Agneessens, and J. Skvoretz, Soc. Networks **32**, 245 (2010).
[23] C. Demetrescu, 9th dimacs implementation challenge - shortest paths, http://archive.dimacs.rutgers.edu/Workshops/Challenge9/.
[24] F. Munoz-Mendez, K. Han, K. Klemmer, and S. Jarvis, *Community Structures, Interactions and Dynamics in London's Bicycle Sharing Network* (ACM Press, New York, NY, 2018).
[25] L. J. LeBlanc, E. K. Morlok, and W. P. Pierskalla, Transportation Research **9**, 309 (1975).
[26] A. Schubert, Scientometrics **53**, 3 (2002).
[27] N. P. Hummon and P. Dereian, Social Networks **11**, 39 (1989).
[28] P. Yodzis, J. Anim. Ecol. **67**, 635 (1998).
[29] R. M. Thompson and A. R. Mcintosh, Ecol Lett. **1**, 200 (1998).
[30] K. Havens, Science **257**, 1107 (1992).
[31] J. Memmott, N. D. Martinez, and J. Cohen, J. Anim. Ecol. **69**, 1 (2000).
[32] J. A. Dunne, R. J. Williams, N. D. Martinez, R. A. Wood, and D. H. Erwin, PLoS Biol. **6**, e102 (2008).
[33] J. Klaise and S. Johnson, Sci. Rep. **7**, 16197 (2017).
[34] J. Bascompte, C. J. Melián, and E. Sala, Proc. Natl. Acad. Sci. USA **102**, 5443 (2005).
[35] R. E. Ulanowicz and D. Baird, J. Marine Syst. **19**, 159 (1999).
[36] R. Ulanowicz and D. L. DeAngelis, in *U.S. Geological Survey Program on the South Florida Ecosystem; Proceedings of South Florida Restoration ScienceForum, May 17–19, 1999, Boca Raton, Florida*, edited by S. Gerould and A. Higher (BiblioGov, 1999) pp. 114–115.
[37] N. D. Martinez, Ecol. Monogr. **61**, 367 (1991).
[38] B. J. Cole, Science **212**, 83 (1981).
[39] D. F. Lott, Z. Tierpsychol. **49**, 418 (1979).
[40] M. W. Schein and M. H. Fohrman, Brit. J. Anim. Behav. **3**, 45 (1955).
[41] T. Grant, Anim. Behav. **21**, 449 (1973).
[42] Y. Takahata, *The Monkeys of Arashiyama: Thirty-five Years of Research in Japan and the West*, edited by L. M. Fedigan and P. J. Asquith (SUNY Press, Albany, 1991) pp. 123–139.
[43] C. C. Hass, J. Zool. **225**, 509 (1991).
[44] J. A. van Hooff and J. A. B. Wensing, in *Man and Wolf: Advances, Issues, and Problems in Captive Wolf Research*, edited by H. Frank (Springer Science & Business Media, 1987) pp. 219–252.
[45] R. M. Thompson and C. Townsend, Oikos **108**, 137 (2005).
[46] J. Link, Mar. Ecol.: Prog. Ser. **230**, 1 (2002).
[47] P. H. Warren, Oikos **55**, 299 (1989).
[48] R. R. Christian and J. J. Luczkovich, Ecol. Modell. **117**, 99 (1999).
[49] L. Goldwasser and J. Roughgarden, Ecology **74**, 1216 (1993).
[50] M. Huxham, S. Beaney, and D. Raffaelli, Oikos **76**, 284 (1996).
[51] M. B. Gerstein, A. Kundaje, M. Hariharan, S. G. Landt, K.-K. Yan, C. Cheng, X. J. Mu, E. Khurana, J. Rozowsky, R. Alexander, *et al.*, Nature (London) **489**, 91 (2012).
[52] D. J. Watts and S. H. Strogatz, Nature (London) **393**, 440 (1998).
[53] D. Thieffry, A. M. Huerta, E. Pérez-Rueda, and J. Collado-Vides, Bioessays **20**, 433 (1998).
[54] H. Salgado, M. Peralta-Gil, S. Gama-Castro, A. Santos-Zavaleta, L. M. niz Rascado, J. S. García-Sotelo, V. Weiss, H. Solano-Lira, I. Martínez-Flores, A. Medina-Rivera, G. Salgado-Osorio, S. Alquicira-Hernández, K. Alquicira-Hernández, A. López-Fuentes, L. Porrón-Sotelo, A. M. Huerta, C. Bonavides-Martínez, Y. I. Balderas-Martínez, L. Pannier, M. Olvera, *et al.*, Nucl. Acids Res. **41**, D203 (2013).
[55] J. Sanz, J. Navarro, A. Arbués, C. Martín, P. C. Marijuán, and Y. Moreno, PLoS ONE **6**, e22178 (2011).
[56] E. Galán-Vásquez, B. Luna, and A. Martínez-Antonio, Microb. Informatics Exp. **1**, 3 (2011).
[57] C. T. Harbison, D. B. Gordon, T. I. Lee, N. K. Rinaldi, K. D. Macisaac, T. W. Danford, N. M. Hannett, J.-B. Tagne, D. B. Reynolds, J. Yoo, E. G. Jennings, J. Zeitlinger, D. K. Pokholok, M. Kellis, P. A. Rolfe, K. T. Takusagawa, E. S.

Lander, D. K. Gifford, E. Fraenkel, and R. A. Young, Nature (London) **431**, 99 (2004).
[58] H. Jeong, B. Tombor, R. Albert, Z. N. Oltvai, and A.-L. Barabási, Nature (London) **407**, 651 (2000).
[59] M. C. Costanzo, M. E. Crawford, J. E. Hirschman, J. E. Kranz, P. Olsen, L. S. Robertson, M. S. Skrzypek, B. R. Braun, K. L. Hopkins, P. Kondu, *et al.*, Nucl. Acids Res. **29**, 75 (2001).
[60] C. Carere, G. F. Ball, and J. Balthazart, J. Comp. Neurol. **500**, 894 (2007).
[61] R. M. Cowell, K. R. Blake, and J. W. Russell, J. Comp. Neurol. **502**, 1 (2007).